Journal of Materials Chemistry C

ROYAL SOCIETY OF CHEMISTRY

PAPER

View Article Online
View Journal | View Issue

Cite this: J. Mater. Chem. C, 2020, 8, 15128

Effects of alkoxylation position on fused-ring electron acceptors†

Jingshuai Zhu,[ab] Yiqun Xiao,[c] Changxi Zhang,[b] Boyu Jia,[b] Heng Lu,[b] Jiayu Wang,[b] Xinhui Lu,[c] Zhen Li *[a] and Xiaowei Zhan *[b]

Received 3rd May 2020,
Accepted 19th May 2020

DOI: 10.1039/d0tc02158j

rsc.li/materials-c

Four fused-ring electron acceptors composed of the same naphtho[1,2-*b*:5,6-*b*′]dithiophene-based core and 3-(1,1-dicyanomethylene)-5,6-difluoro-1-indanone end groups without or with hexyloxyl groups on the core and/or phenyl side chains are compared to systematically study the effects of alkoxylation position on the molecular packing, optical, electronic, and photovoltaic properties of the nonfullerene acceptors. Alkoxylation on the core red-shifts absorption and reduces bandgap, while that on side chains has little effect on absorption and bandgap. Alkoxylation on the core up-shifts the HOMO and down-shifts the LUMO, while that on side chains shows very little effect on the energy levels. Alkoxylation on the core slightly improves electron mobility relative to that on the side chains. Both methods of alkoxylation decrease open-circuit voltage, but increase short-circuit current density and fill factor, leading to improved efficiencies of the organic solar cells. Finally, when blended with the polymer donor **PM6**, **IOIC3**/**IOIC4** with alkoxylation on the core or side chains yields efficiencies of 11.1–12.8%, which are higher than that of **IOIC2** without alkoxylation (10.5%). **IOIC5** with alkoxylation on both the core and side chains yields the highest efficiency of 13.8%.

Introduction

Organic solar cells (OSCs) are considered to be one of the promising next-generation solar energy technologies because they present unique features, such as being light-weight, flexibility, portability, semi-transparency, and fast mass production by roll-to-roll printing, and therefore they have received widespread attention in the last 30 years.[1–9] Fullerene derivatives (*e.g.*, $PC_{61}BM$ and $PC_{71}BM$) have been traditional electron acceptors in bulk heterojunction (BHJ) OSCs, and power conversion efficiencies (PCEs) of up to 12% have been achieved for the fullerene-based devices.[10,11] However, fullerene acceptors suffer from several shortcomings, such as insufficient absorption in the visible and near infrared (NIR) regions, morphological instability, and limited adjustability of energy levels, which constrain the sustainable development of OSCs.[12–14] In consequence, nonfullerene acceptors have been developed as alternatives to overcome these deficiencies of fullerene acceptors.[15–21]

In 2015, we reported a series of high-performance fused-ring electron acceptors (FREAs) represented by the star molecule ITIC.[22] Since then, the development of the FREA family has flourished, and the OSCs based on FREAs have continually broken PCE records that are over 18% now.[23–32] FREAs feature several advantages, such as facile synthesis, variable energy levels to fit various donor materials, a strong photoresponse in the visible-NIR regions, high exciton diffusion coefficients, 3D exciton and charge transport, and excellent stability.[33–39] Most endeavors to enhance the performance of FREAs have focused on modifications of fused-ring cores,[40–43] side chains,[44–48] and end groups.[49–52]

Modification of the side chains has also been widely used to optimize the performance of FREAs through affecting the optoelectric properties and film morphology.[53,54] For example, introducing alkoxyl groups onto phenyl side chains[55–58] or central cores[44,59–61] can not only modulate energy levels and enhance absorption, but also regulate morphology and enhance charge mobility of the FREAs. Nevertheless, there have been no works that compared the effects of alkoxyl substituents located on the core and side chains of FREAs on their performance.

In this work, we construct a small family of homologous FREAs consisting of the same core, naphtho[1,2-*b*:5,6-*b*′]dithiophene (NDT) condensed with two cyclopentadienylthiophenes,

[a] Department of Chemistry, Hubei Key Lab on Organic and Polymeric, Opto-Electronic Materials, Wuhan University, Wuhan 430072, China. E-mail: lizhen@whu.edu.cn
[b] Department of Materials Science and Engineering, College of Engineering, Key Laboratory of Polymer Chemistry and Physics of Ministry of Education, Peking University, Beijing 100871, China. E-mail: xwzhan@pku.edu.cn
[c] Department of Physics, The Chinese University of Hong Kong, New Territories 999077, Hong Kong, China

† Electronic supplementary information (ESI) available: Synthesis and characterization, device fabrication, absorption, UPS, SCLC, AFM, TEM, GIWAXS, GISAXS and OSC data. See DOI: 10.1039/d0tc02158j

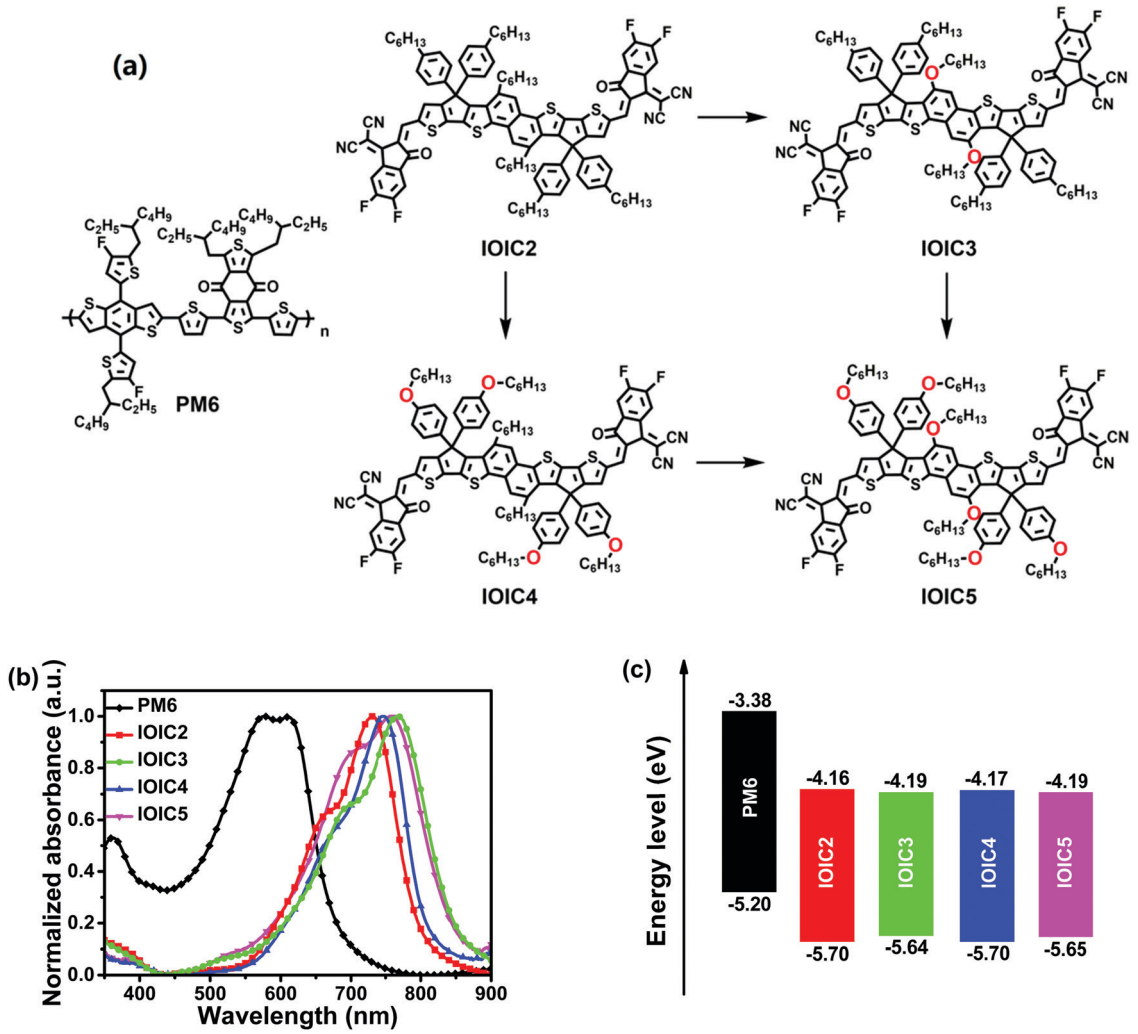

Fig. 1 (a) Chemical structures, (b) thin-film absorption spectra, and (c) energy levels of **PM6** and the IOIC series.

and the same end groups, 3-(1,1-dicyanomethylene)-5,6-difluoro-1-indanone (2FIC), without or with hexyloxyl groups on the core and/or side chains, to systematically probe the impacts of alkoxylation position on the properties of the FREAs. In our previous work, we synthesized **IOIC2** with hexyl groups on the core and the side chains (Fig. 1a).[62] Then, we synthesized **IOIC3** (Fig. 1a) by replacing the hexyl groups on the core of **IOIC2** with hexyloxyl groups.[59] Herein, we used hexyloxyl to replace hexyl groups on the phenyl side chains of **IOIC2**, and synthesized **IOIC4** (Fig. 1a); we used hexyloxyl to replace the hexyl groups on the core and the phenyl side chains of **IOIC2**, and synthesized **IOIC5** (Fig. 1a). The alkoxylation on the core results in bathochromic-shifted absorption spectra and a reduced optical bandgap, while the alkoxylation on the side chains has little effects on the absorption and bandgap. The alkoxylation on the core up-shifts the highest occupied molecular orbital (HOMO) level and down-shifts the lowest unoccupied molecular orbital (LUMO) level, while the alkoxylation on the side chains has little effects on the energy levels. The alkoxylation on the core slightly increases electron mobility, while the alkoxylation on the side chains has little effects on electron mobility. OSCs based on the IOIC series and the wide-bandgap polymer donor **PM6**[63] (Fig. 1a) yield PCEs of 10.5% to 13.8%. Both methods of alkoxylation on the core and side chains improve the PCEs; by combining both the core and side-chain alkoxylation methods, the highest PCE of 13.8% is found with **IOIC5**.

Results and discussion

Material synthesis and characterization

The synthetic routes of **IOIC4** and **IOIC5** are shown in Scheme S1 (ESI†), and the detailed synthesis procedures are provided in the ESI.† The molecular structures of **IOIC4** and **IOIC5** were confirmed through ^{1}H NMR spectroscopy, ^{13}C NMR spectroscopy, mass spectrometry, and elemental analysis (see ESI†). The normalized optical absorption spectra of the IOIC series of compounds in chloroform solution (10^{-6} M) are shown in Fig. S1 (ESI†); all compounds have similar maximum molar extinction coefficients of 1.6–1.9 $\times$ 10^{5} M^{-1} cm^{-1}. In the thin films,

Table 1 Basic properties of the IOIC series

Compound	λ_{max} (nm) Solution	Film	ε (M^{-1} cm^{-1})	E_g (eV)	HOMO (eV)	LUMO (eV)	μ_e (10^{-3} cm^2 V^{-1} s^{-1})
IOIC2	696	730	1.8×10^5	1.54	−5.70	−4.16	1.0
IOIC3	715	765	1.9×10^5	1.45	−5.64	−4.19	1.5
IOIC4	698	748	1.6×10^5	1.53	−5.70	−4.17	1.1
IOIC5	718	758	1.9×10^5	1.46	−5.65	−4.19	1.5

IOIC2, **IOIC3**, **IOIC4** and **IOIC5** show absorption peaks at 730, 765, 748 and 758 nm, respectively (Fig. 1b); their optical bandgap (E_g) values are 1.45–1.54 eV (Table 1). Compared with **IOIC2** without hexyloxyl groups, **IOIC3** with hexyloxyl groups on the core shows markedly red-shifted absorption and a narrower E_g, while **IOIC4** with hexyloxyl groups on the side chains shows slightly red-shifted absorption and a similar E_g.

We used ultraviolet photoelectron spectroscopy (UPS) to measure the energy levels of the IOIC series of films (Fig. S2, ESI†). The HOMO levels of **IOIC2**, **IOIC3**, **IOIC4** and **IOIC5** measured by UPS are −5.70 eV, −5.64 eV, −5.70 eV and −5.65 eV, respectively (Fig. 1c); from the HOMO and E_g, the LUMO levels were determined to be −4.16 eV, −4.19 eV, −4.17 eV and −4.19 eV, respectively. Compared with **IOIC2** without hexyloxyl groups, **IOIC3** with hexyloxyl groups on the core shows an up-shifted HOMO and down-shifted LUMO, while **IOIC4** with hexyloxyl groups on the side chains shows a very similar HOMO/LUMO.

Space charge limited current (SCLC) measurements (Fig. S3, ESI†) were used to study the IOIC series as neat films. Compared with **IOIC2** without hexyloxyl groups (1.0×10^{-3} cm^2 V^{-1} s^{-1}), **IOIC4** with hexyloxyl groups on the side chains has a similar electron mobility of 1.1×10^{-3} cm^2 V^{-1} s^{-1}, while **IOIC3** and **IOIC5** with hexyloxyl groups on the core have slightly higher electron mobilities of 1.5×10^{-3} cm^2 V^{-1} s^{-1}.

Photovoltaic properties

The mid-bandgap polymer donor **PM6** and the four FREAs exhibit complementary absorption in the 350–850 nm region (Fig. 1b) and the energy levels of **PM6** fit those of the IOIC series of acceptors (Fig. 1c). Thus, BHJ OSCs were fabricated with a structure of indium tin oxide (ITO)/ZnO/**PM6**:acceptor/MoO_3/Ag. The effects of donor/acceptor (D/A) weight ratio and 1,8-diiodooctane (DIO) additive content on the device performance were investigated, and the optimization details are summarized in Tables S1 and S2 (ESI†).

The current density–voltage (J–V) curves of the optimal devices based on the IOIC series are shown in Fig. 2a. The open-circuit voltage (V_{OC}), short-circuit current density (J_{SC}), fill factor (FF), and PCE of the best cells are listed in Table 2. The V_{OC} of the **IOIC2**, **IOIC3**, **IOIC4** and **IOIC5**-based cells is 0.970, 0.920, 0.964 and 0.920 V, respectively. The effects of hexyloxyl substituents on the core and phenyl side chains are responsible for different trends in V_{OC}. The hexyloxyls on the core lead to a smaller V_{OC}; taking **IOIC2**/**IOIC3** as an example, the V_{OC} decreases by 0.05 V upon alkyloxylation; a similar decrease is observed on going from **IOIC4** to **IOIC5**. This decrease in V_{OC} is caused by the down-shift of LUMO upon alkyloxylation of the core. In contrast, hexyloxyl substituents on the phenyl side chains have little effect on the V_{OC}; very similar V_{OC} values were found for **IOIC2**/**IOIC4** or **IOIC3**/**IOIC5**. This trend is also in accordance with the LUMO, which is almost completely unaffected by the presence of hexyloxyls on the side chains.

J_{SC} varies from 16.3 to 20.9 mA cm^{-2}, and alkyloxylation on either the core or side chains leads to a higher J_{SC}. The J_{SC} also depends on the alkyloxylation position. When comparing the **IOIC2**–**IOIC4** series, both hexyloxylated acceptors **IOIC3**/**IOIC4** have a higher J_{SC} than **IOIC2**; however, hexyloxyl substituents on the core (**IOIC3**, J_{SC} = 20.0 mA cm^{-2}, a 23% improvement) lead to a larger increase than on the side chains (**IOIC4**, J_{SC} = 17.3 mA cm^{-2}, a 6% improvement). The external quantum efficiency (EQE) spectra of the best cells are shown in Fig. 2b. A similar trend was found: alkyloxylation leads to higher EQE values and core alkyloxylation leads to a larger increase than that of side-chain alkyloxylation. These trends in J_{SC} and EQE are consistent with the absorption spectra in which the side-chain alkyloxylation does not cause a notable red-shift that is observed with core alkyloxylation.

The FF varies from 66.1% to 71.5%, and alkyloxylation on either the core or side chains leads to a higher FF. The FF is also sensitive to the alkyloxylation position. In the **IOIC2**–**IOIC4** series, both hexyloxylated acceptors **IOIC3**/**IOIC4** have a higher FF than **IOIC2**; however, hexyloxyl substituents on the core (**IOIC3**, FF = 69.7%) lead to a larger increase than on the side chains (**IOIC4**, J_{SC} = 66.7%). Finally, when both core and side chains are alkyloxylated, the highest FF of 71.5% is found for **IOIC5**. The charge mobilities of the blends were measured by using the SCLC method (Fig. S4 and Table S3, ESI†). The hole mobilities of all the blends are on the same magnitude ($1.6–4.5 \times 10^{-4}$ cm^2 V^{-1} s^{-1}), while the highest μ_e is found for the **IOIC5** blend, contributing to the highest FF.

Finally, the increase in the J_{SC} and FF outweighs the decrease in V_{OC}, which are caused by alkyloxylation, leading to a PCE enhancement from 10.5% to 13.8%. When comparing **IOIC3** (core alkyloxylation, PCE = 12.8%) to **IOIC4** (side-chain alkyloxylation, PCE = 11.1%), the large increase in J_{SC} from core alkyloxylation drives the higher PCE. However, compared to **IOIC2** without hexyloxyls (PCE = 10.5%), both methods of alkyloxylation lead to an overall increase in PCE. Additionally, by combining both core and side-chain alkyloxylation methods, the highest PCE of 13.8% is found with **IOIC5**.

Variation of photocurrent density (J_{ph}) with effective voltage (V_{eff}) was investigated to probe the charge extraction properties (Fig. 2c).[64] J_{ph} of the devices approaches saturation (J_{sat}) under

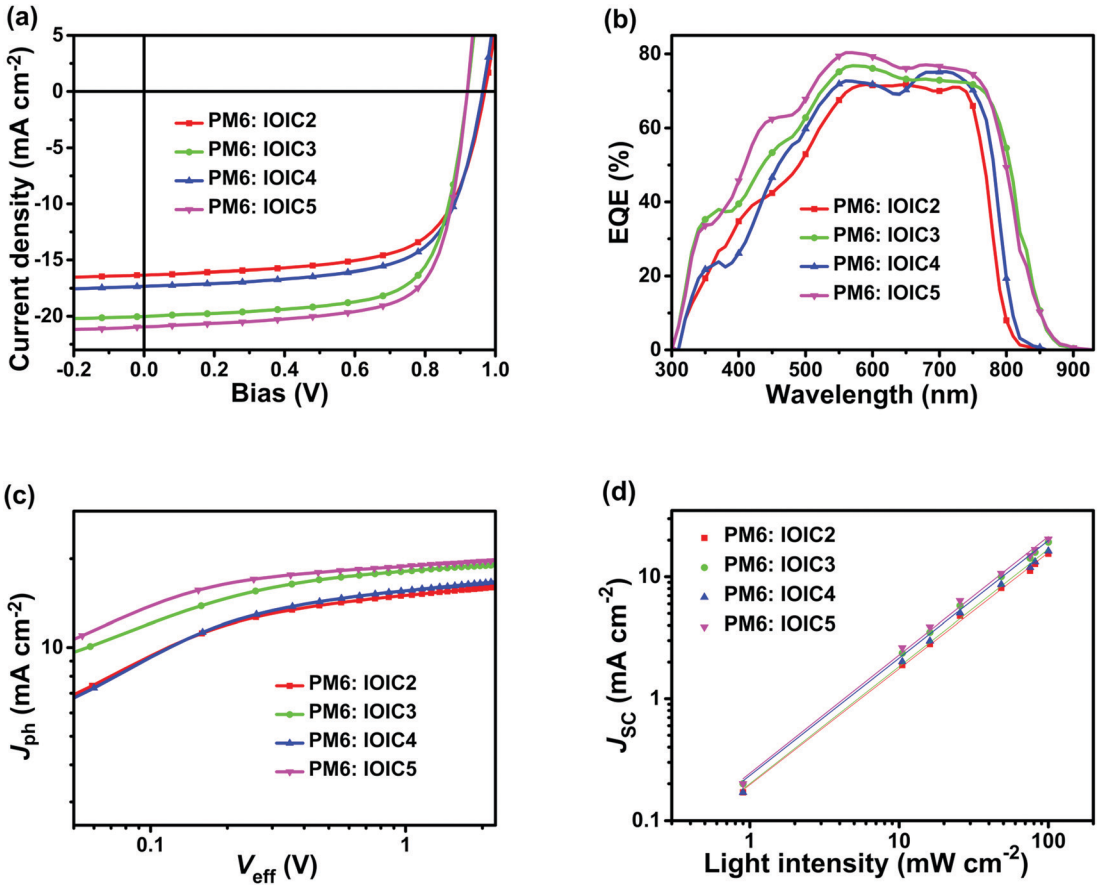

Fig. 2 (a) J–V curves, (b) EQE spectra, (c) J_{ph} *versus* V_{eff} characteristics, and (d) J_{SC} *versus* light intensity of optimized devices based on **PM6**:acceptors.

Table 2 Best photovoltaic performance of OSCs based on **PM6**:acceptors (average data are obtained from 20 devices, best data in brackets)

Active layer	V_{OC} (V)	J_{SC} (mA cm^{-2})	FF (%)	PCE (%)	Calculated J_{SC} (mA cm^{-2})
PM6:IOIC2	0.972 ± 0.006 (0.970)	16.1 ± 0.4 (16.3)	64.7 ± 1.3 (66.1)	10.1 ± 0.2 (10.5)	15.9
PM6:IOIC3	0.921 ± 0.003 (0.920)	19.7 ± 0.8 (20.0)	68.6 ± 0.9 (69.7)	12.5 ± 0.4 (12.8)	19.3
PM6:IOIC4	0.966 ± 0.007 (0.964)	17.0 ± 0.5 (17.3)	65.1 ± 1.7 (66.7)	10.7 ± 0.3 (11.1)	17.0
PM6:IOIC5	0.922 ± 0.005 (0.920)	20.5 ± 0.7 (20.9)	70.5 ± 1.4 (71.5)	13.4 ± 0.3 (13.8)	20.3

$V_{eff} > 2$ V; the value of J_{SC}/J_{sat} can reflect the degree of charge extraction. The J_{SC}/J_{sat} values of the devices based on **IOIC2**, **IOIC3**, **IOIC4** and **IOIC5** are 0.94, 0.95, 0.94 and 0.96, respectively, suggesting efficient charge extraction in all devices and slightly better charge extraction for **IOIC5**.

We also measured J_{SC} under different incident light intensity (P_{light}) to study the charge recombination behavior (Fig. 2d), and the correlation between J_{SC} and P_{light} is expressed by $J_{SC} \propto P_{light}^{\alpha}$.[65] For **IOIC2**, **IOIC3**, **IOIC4** and **IOIC5** based devices, the values of α are estimated to be 0.95, 0.96, 0.96 and 0.97 under short-circuit conditions, respectively, suggesting weak bimolecular charge recombination in all devices and slightly better bimolecular charge recombination in **IOIC5**.

Film morphology

The morphology of the blended films was studied by using atomic force microscopy (AFM) and transmission electron microscopy (TEM). In the AFM images (Fig. S5, ESI†), all the blends present fibril features (about 15–20 nm in diameter) with a large root-mean-square roughness (R_q) of 7.90–8.68 nm. As can be seen from the TEM images (Fig. S6, ESI†), all the blend films present dense and continuous networks.

To study how the alkoxylation position affects the crystalline packing of the thin films, grazing-incidence wide-angle X-ray scattering (GIWAXS) was employed.[66,67] The two-dimensional (2D) GIWAXS patterns and the corresponding intensity profiles along the in-plane and out-of-plane directions of the pure and

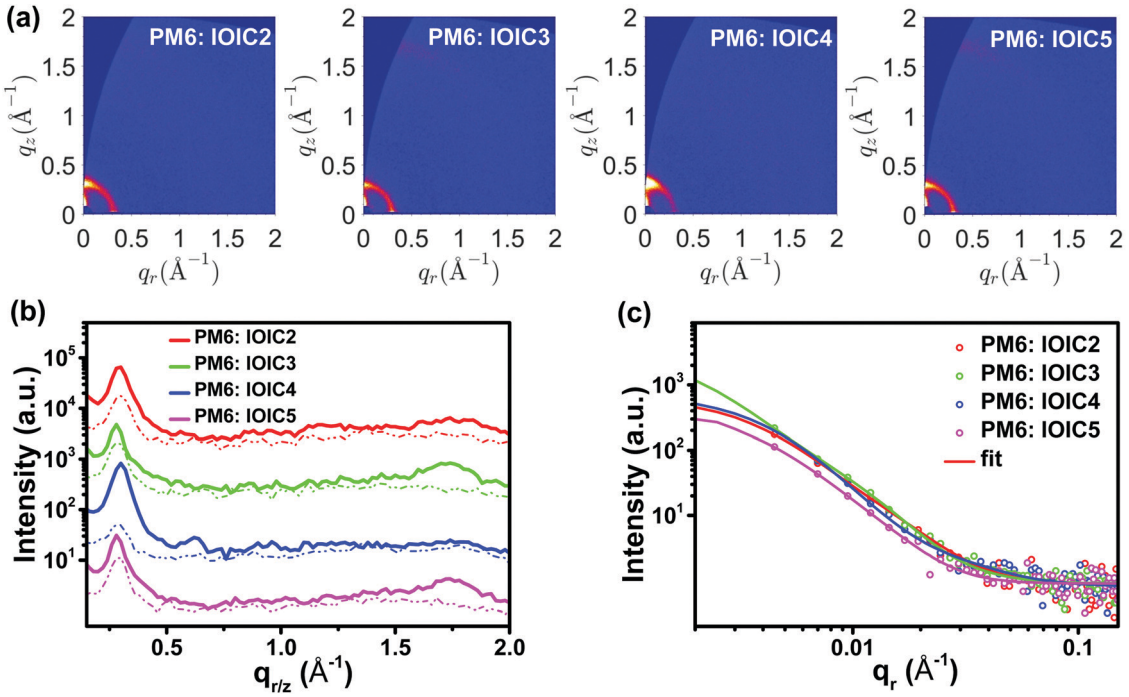

Fig. 3 (a) 2D GIWAXS patterns and (b) in-plane (dashed lines) and out-of-plane (solid lines) scattering profiles for the blended films, and (c) the in-plane GISAXS profiles for the blended films.

blend films are presented in Fig. S7 (ESI†) and Fig. 3a, b, respectively. The pure **IOIC4** film is preferentially edge-on oriented with the (100) lamellar peak concentrated at q_z = 0.31 Å^{-1}. The pure **IOIC2** film is bimodal with strong egde-on and weak face-on order. In contrast, pure **IOIC3** and **IOIC5** films exhibit preferential "face-on" stacking features with the lamellar peak located at q_r = 0.29 Å^{-1} and 0.31 Å^{-1} and the π–π peak at q_z = 1.74 Å^{-1} and 1.78 Å^{-1}, respectively (Fig. S7, ESI†), contributing to higher electron mobilities relative to those of **IOIC2** and **IOIC4** in neat films. Consequently, the **PM6:IOIC4** blend films exhibit the strongest "edge-on" orientation with the lamellar peak at q_z = 0.30 Å^{-1} (d = 20.9 Å) compared with the other blend films. This is expected to be unfavorable for vertical charge transport; both μ_h and μ_e are indeed lower in the blend. The **PM6:IOIC2** film presents a weaker edge-on orientation, with a ring-like lamellar peak located at q = 0.30 Å^{-1}. There was no obvious π–π peak identified for the **PM6:IOIC2** and **PM6:IOIC4** films. The **PM6:IOIC3** and **PM6:IOIC5** blend films exhibit a dominant "face-on" orientation with a lamellar peak appearing at q_r = 0.30 Å^{-1} (d = 20.9 Å) and the π–π peak at q_z = 1.72 Å^{-1}. Based on Scherrer's equation,[68] the crystallite coherence lengths (CCLs) of the lamellar peaks of the **PM6:IOIC3** and **PM6:IOIC5** blend films are calculated to be 79.4 Å and 84.5 Å, respectively, and the corresponding CCLs of the π–π peaks are 27.8 Å and 33.5 Å.

Besides, grazing-incidence small-angle X-ray scattering (GISAXS) measurements were also performed to study the domain sizes of the blend films. The in-plane intensity profiles and best fittings are presented in Fig. 3c. Using the Debye–Anderson–Brumberger (DAB) model, the correlation lengths of the amorphous intermixing phases were fitted to be 16.4, 15.2, 19.4 and 18.7 nm for the **IOIC2**, **IOIC3**, **IOIC4** and **IOIC5** blend films. The acceptor domain sizes were fitted using the fractal-like network, and were found to be 19.4, 6.0, 7.5 and 20.4 nm for the **IOIC2**, **IOIC3**, **IOIC4** and **IOIC5** blend films, respectively. Despite all the blend films having appropriate pure acceptor domain sizes for exciton dissociation, a relatively larger acceptor domain size, such as in the **IOIC2** and **IOIC5** blend films, could more easily form connected pathways for electron transport. Thus, the **PM6:IOIC5** film exhibits the largest CCLs, a favorable face-on orientation and connected electron transport pathways, consistent with the observed higher mobilities and FF.

Conclusion

Based on the same NDT-based core and 2FIC end groups, four IOIC compounds with/without hexyloxyls on the core and/or side chains were compared to probe the effects of alkoxylation position on their absorption, energy levels, charge transport, film morphology and photovoltaic performance. The main effects of alkoxylation are summarized as follows. (a) Alkoxylation on the core red-shifts the absorption spectrum and reduces the bandgap, while alkoxylation on the side chains has little impact on the absorption and bandgap. (b) Alkoxylation on the core up-shifts the HOMO due to the π-conjugative effect of the hexyloxyls and down-shifts the LUMO due to the σ-inductive effect of the hexyloxyls; while alkoxylation on the side chains shows very little effect on the energy levels. (c) Alkoxylation on

the core leads to a slightly higher electron mobility due to higher molecular ordering relative to the side-chain alkoxylation. (d) Compared to **IOIC2** without hexyloxyls, both methods of alkyloxylation enhance PCE; the core alkyloxylation leads to a larger increase than that on the side chains primarily due to the larger increase in J_{SC}. Finally, by combining both side-chain and core alkyloxylation methods, the highest PCE of 13.8% is achieved with **IOIC5**. These results demonstrate that alkyloxylation location has notable impacts on the molecular packing and basic properties of the FREAs and alkyloxylation on both core and side chains is an effective approach towards high-efficiency nonfullerene acceptors.

Conflicts of interest

There are no conflicts of interest to declare.

Acknowledgements

X. Z. thanks NSFC (Grant No. 21734001 and 51761165023), Z. L. thanks NSFC (Grant No. 21734007), and X. L. acknowledges the financial support from NSFC/RGC Joint Research Scheme (Grant No. N_CUHK418/17).

Notes and references

1 Y. Li, *Acc. Chem. Res.*, 2012, **45**, 723–733.
2 G. Li, R. Zhu and Y. Yang, *Nat. Photon.*, 2012, **6**, 153–161.
3 A. J. Heeger, *Adv. Mater.*, 2014, **26**, 10–28.
4 Y.-J. Cheng, S.-H. Yang and C.-S. Hsu, *Chem. Rev.*, 2009, **109**, 5868–5923.
5 Y. Lin and X. Zhan, *Acc. Chem. Res.*, 2016, **49**, 175–183.
6 G. Dennler, M. C. Scharber and C. J. Brabec, *Adv. Mater.*, 2009, **21**, 1323–1338.
7 F. C. Krebs, N. Espinosa, M. Hösel, R. R. Søndergaard and M. Jørgensen, *Adv. Mater.*, 2014, **26**, 29–39.
8 L. Lu, T. Zheng, Q. Wu, A. M. Schneider, D. Zhao and L. Yu, *Chem. Rev.*, 2015, **115**, 12666–12731.
9 D. Han, T. Kumari, S. Jung, Y. An and C. Yang, *Sol. RRL*, 2018, **2**, 1800009.
10 J. Zhao, Y. Li, G. Yang, K. Jiang, H. Lin, H. Ade, W. Ma and H. Yan, *Nat. Energy*, 2016, **1**, 15027.
11 G. Yu, J. Gao, J. C. Hummelen, F. Wudl and A. J. Heeger, *Science*, 1995, **270**, 1789–1791.
12 C. Yan, S. Barlow, Z. Wang, H. Yan, A. K. Y. Jen, S. R. Marder and X. Zhan, *Nat. Rev. Mater.*, 2018, **3**, 18003.
13 J. Hou, O. Inganäs, R. H. Friend and F. Gao, *Nat. Mater.*, 2018, **17**, 119–128.
14 P. Cheng, G. Li, X. Zhan and Y. Yang, *Nat. Photon.*, 2018, **12**, 131–142.
15 Y. Lin, Q. He, F. Zhao, L. Huo, J. Mai, X. Lu, C.-J. Su, T. Li, J. Wang, J. Zhu, Y. Sun, C. Wang and X. Zhan, *J. Am. Chem. Soc.*, 2016, **138**, 2973–2976.
16 W. Wang, C. Yan, T. K. Lau, J. Wang, K. Liu, Y. Fan, X. Lu and X. Zhan, *Adv. Mater.*, 2017, **29**, 1701308.
17 X. Zhan, Z. Tan, B. Domercq, Z. An, X. Zhang, S. Barlow, Y. Li, D. Zhu, B. Kippelen and S. R. Marder, *J. Am. Chem. Soc.*, 2007, **129**, 7246–7247.
18 J. Sun, X. Ma, Z. Zhang, J. Yu, J. Zhou, X. Yin, L. Yang, R. Geng, R. Zhu, F. Zhang and W. Tang, *Adv. Mater.*, 2018, **30**, 1707150.
19 Q. Wu, D. Zhao, A. M. Schneider, W. Chen and L. Yu, *J. Am. Chem. Soc.*, 2016, **138**, 7248–7251.
20 G. Zhang, J. Zhao, P. C. Y. Chow, K. Jiang, J. Zhang, Z. Zhu, J. Zhang, F. Huang and H. Yan, *Chem. Rev.*, 2018, **118**, 3447–3507.
21 A. Wadsworth, M. Moser, A. Marks, M. S. Little, N. Gasparini, C. J. Brabec, D. Baran and I. McCulloch, *Chem. Soc. Rev.*, 2019, **48**, 1596–1625.
22 Y. Lin, J. Wang, Z.-G. Zhang, H. Bai, Y. Li, D. Zhu and X. Zhan, *Adv. Mater.*, 2015, **27**, 1170–1174.
23 Q. Liu, Y. Jiang, K. Jin, J. Qin, J. Xu, W. Li, J. Xiong, J. Liu, Z. Xiao, K. Sun, S. Yang, X. Zhang and L. Ding, *Sci. Bull.*, 2020, **65**, 272–275.
24 X. Xu, K. Feng, Z. Bi, W. Ma, G. Zhang and Q. Peng, *Adv. Mater.*, 2019, **31**, 1901872.
25 L. Hong, H. Yao, Z. Wu, Y. Cui, T. Zhang, Y. Xu, R. Yu, Q. Liao, B. Gao, K. Xian, H. Y. Woo, Z. Ge and J. Hou, *Adv. Mater.*, 2019, **31**, 1903441.
26 S. Liu, J. Yuan, W. Deng, M. Luo, Y. Xie, Q. Liang, Y. Zou, Z. He, H. Wu and Y. Cao, *Nat. Photon.*, 2020, **14**, 300–305.
27 J. Yuan, Y. Zhang, L. Zhou, G. Zhang, H.-L. Yip, T.-K. Lau, X. Lu, C. Zhu, H. Peng, P. A. Johnson, M. Leclerc, Y. Cao, J. Ulanski, Y. Li and Y. Zou, *Joule*, 2019, **3**, 1140–1151.
28 Z. Zhou, W. Liu, G. Zhou, M. Zhang, D. Qian, J. Zhang, S. Chen, S. Xu, C. Yang, F. Gao, H. Zhu, F. Liu and X. Zhu, *Adv. Mater.*, 2020, **32**, 1906324.
29 J. Wang, J. Zhang, Y. Xiao, T. Xiao, R. Zhu, C. Yan, Y. Fu, G. Lu, X. Lu, S. R. Marder and X. Zhan, *J. Am. Chem. Soc.*, 2018, **140**, 9140–9147.
30 D. Baran, R. S. Ashraf, D. A. Hanifi, M. Abdelsamie, N. Gasparini, J. A. Rohr, S. Holliday, A. Wadsworth, S. Lockett, M. Neophytou, C. J. Emmott, J. Nelson, C. J. Brabec, A. Amassian, A. Salleo, T. Kirchartz, J. R. Durrant and I. McCulloch, *Nat. Mater.*, 2017, **16**, 363–369.
31 L. Meng, Y. Zhang, X. Wan, C. Li, X. Zhang, Y. Wang, X. Ke, Z. Xiao, L. Ding, R. Xia, H.-L. Yip, Y. Cao and Y. Chen, *Science*, 2018, **361**, 1094–1098.
32 X. Che, Y. Li, Y. Qu and S. R. Forrest, *Nat. Energy*, 2018, **3**, 422–427.
33 S. Dai, T. Li, W. Wang, Y. Xiao, T.-K. Lau, Z. Li, K. Liu, X. Lu and X. Zhan, *Adv. Mater.*, 2018, **30**, 1706571.
34 S. Chandrabose, K. Chen, A. Barker, J. Sutton, S. Prasad, J. Zhu, J. Zhou, K. Gordon, Z. Xie, X. Zhan and J. M. Hodgkiss, *J. Am. Chem. Soc.*, 2019, **141**, 6922–6929.
35 S. Dai, J. Zhou, S. Chandrabose, Y. Shi, G. Han, K. Chen, J. Xin, K. Liu, Z. Chen, Z. Xie, W. Ma, Y. Yi, L. Jiang, J. M. Hodgkiss and X. Zhan, *Adv. Mater.*, 2020, **32**, 2000645.
36 Y. Lin, Z.-G. Zhang, H. Bai, J. Wang, Y. Yao, Y. Li, D. Zhu and X. Zhan, *Energy Environ. Sci.*, 2015, **8**, 610–616.
37 T. Li, S. Dai, Z. Ke, L. Yang, J. Wang, C. Yan, W. Ma and X. Zhan, *Adv. Mater.*, 2018, **30**, 1705969.

38 Y. Lin, F. Zhao, S. K. K. Prasad, J.-D. Chen, W. Cai, Q. Zhang, K. Chen, Y. Wu, W. Ma, F. Gao, J.-X. Tang, C. Wang, W. You, J. M. Hodgkiss and X. Zhan, *Adv. Mater.*, 2018, **30**, 1706363.
39 Y. Lin, F. Zhao, Y. Wu, K. Chen, Y. Xia, G. Li, S. K. K. Prasad, J. Zhu, L. Huo, H. Bin, Z.-G. Zhang, X. Guo, M. Zhang, Y. Sun, F. Gao, Z. Wei, W. Ma, C. Wang, J. Hodgkiss, Z. Bo, O. Inganäs, Y. Li and X. Zhan, *Adv. Mater.*, 2017, **29**, 1604155.
40 G. Cai, W. Wang, J. Zhou, Y. Xiao, K. Liu, Z. Xie, X. Lu, J. Lian, P. Zeng, Y. Wang and X. Zhan, *ACS Mater. Lett.*, 2019, **1**, 367–374.
41 Z. Yao, X. Liao, K. Gao, F. Lin, X. Xu, X. Shi, L. Zuo, F. Liu, Y. Chen and A. K.-Y. Jen, *J. Am. Chem. Soc.*, 2018, **140**, 2054–2057.
42 B. Kan, H. Feng, X. Wan, F. Liu, X. Ke, Y. Wang, Y. Wang, H. Zhang, C. Li, J. Hou and Y. Chen, *J. Am. Chem. Soc.*, 2017, **139**, 4929–4934.
43 B. Jia, J. Wang, Y. Wu, M. Zhang, Y. Jiang, Z. Tang, T. P. Russell and X. Zhan, *J. Am. Chem. Soc.*, 2019, **141**, 19023–19031.
44 Y. Li, L. Zhong, B. Gautam, H.-J. Bin, J.-D. Lin, F.-P. Wu, Z. Zhang, Z.-Q. Jiang, Z.-G. Zhang, K. Gundogdu, Y. Li and L.-S. Liao, *Energy Environ. Sci.*, 2017, **10**, 1610–1620.
45 Y. Li, N. Zheng, L. Yu, S. Wen, C. Gao, M. Sun and R. Yang, *Adv. Mater.*, 2019, **31**, 1807832.
46 Z. Fei, F. D. Eisner, X. Jiao, M. Azzouzi, J. A. Rohr, Y. Han, M. Shahid, A. S. R. Chesman, C. D. Easton, C. R. McNeill, T. D. Anthopoulos, J. Nelson and M. Heeney, *Adv. Mater.*, 2018, **30**, 1705209.
47 Y. Lin, F. Zhao, Q. He, L. Huo, Y. Wu, T. C. Parker, W. Ma, Y. Sun, C. Wang, D. Zhu, A. J. Heeger, S. R. Marder and X. Zhan, *J. Am. Chem. Soc.*, 2016, **138**, 4955–4961.
48 J. Lee, E. M. Go, S. Dharmapurikar, J. Xu, S. M. Lee, M. Jeong, K. C. Lee, J. Oh, Y. Cho, C. Zhang, M. Xiao, S. K. Kwak and C. Yang, *J. Mater. Chem. A*, 2019, **7**, 18468–18479.
49 H. Yao, L. Ye, J. Hou, B. Jang, G. Han, Y. Cui, G. M. Su, C. Wang, B. Gao, R. Yu, H. Zhang, Y. Yi, H. Y. Woo, H. Ade and J. Hou, *Adv. Mater.*, 2017, **29**, 1700254.
50 T. Aldrich, M. Matta, W. Zhu, S. Swick, C. Stern, G. Schatz, A. Facchetti, F. Melkonyan and T. Marks, *J. Am. Chem. Soc.*, 2019, **141**, 3274–3287.
51 S. Dai, F. Zhao, Q. Zhang, T.-K. Lau, T. Li, K. Liu, Q. Ling, C. Wang, X. Lu, W. You and X. Zhan, *J. Am. Chem. Soc.*, 2017, **139**, 1336–1343.
52 D. Xie, T. Liu, W. Gao, C. Zhong, L. Huo, Z. Luo, K. Wu, W. Xiong, F. Liu, Y. Sun and C. Yang, *Sol. RRL*, 2017, **1**, 1700044.
53 Y. Yang, Z.-G. Zhang, H. Bin, S. Chen, L. Gao, L. Xue, C. Yang and Y. Li, *J. Am. Chem. Soc.*, 2016, **138**, 15011–15018.
54 J. Wang, W. Wang, X. Wang, Y. Wu, Q. Zhang, C. Yan, W. Ma, W. You and X. Zhan, *Adv. Mater.*, 2017, **29**, 1702125.
55 Z. Zhang, H. Wang, J. Yu, R. Sun, J. Xu, L. Yang, R. Geng, J. Cao, F. Du, J. Min, F. Liu and W. Tang, *Chem. Mater.*, 2020, **32**, 1297–1307.
56 H. Feng, X. Song, Z. Zhang, R. Geng, J. Yu, L. Yang, D. Baran and W. Tang, *Adv. Funct. Mater.*, 2019, **29**, 1903269.
57 W. Su, Q. Fan, X. Guo, J. Chen, Y. Wang, X. Wang, P. Dai, C. Ye, X. Bao, W. Ma, M. Zhang and Y. Li, *J. Mater. Chem. A*, 2018, **6**, 7988–7996.
58 S. Lee, K. H. Park, J.-H. Lee, H. Back, M. J. Sung, J. Lee, J. Kim, H. Kim, Y.-H. Kim, S.-K. Kwon and K. Lee, *Adv. Energy Mater.*, 2019, **9**, 1900044.
59 J. Zhu, Y. Xiao, J. Wang, K. Liu, H. Jiang, Y. Lin, X. Lu and X. Zhan, *Chem. Mater.*, 2018, **30**, 4150–4156.
60 Y. Sun, H.-H. Gao, Y.-Q.-Q. Yi, X. Wan, H. Feng, X. Ke, Y. Zhang, J. Yan, C. Li and Y. Chen, *Sci. China Mater.*, 2019, **62**, 1210–1217.
61 X. Dong, Q. Guo, Q. Liu, L. Zhu, X. Guo, F. Liu and M. Zhang, *J. Mater. Chem. C*, 2020, **8**, 6513–6520.
62 J. Zhu, Z. Ke, Q. Zhang, J. Wang, S. Dai, Y. Wu, Y. Xu, Y. Lin, W. Ma, W. You and X. Zhan, *Adv. Mater.*, 2018, **30**, 1704713.
63 M. Zhang, X. Guo, W. Ma, H. Ade and J. Hou, *Adv. Mater.*, 2015, **27**, 4655–4660.
64 M. A. Faist, S. Shoaee, S. Tuladhar, G. F. A. Dibb, S. Foster, W. Gong, T. Kirchartz, D. D. C. Bradley, J. R. Durrant and J. Nelson, *Adv. Energy Mater.*, 2013, **3**, 744–752.
65 I. Riedel, J. Parisi, V. Dyakonov, L. Lutsen, D. Vanderzande and J. C. Hummelen, *Adv. Funct. Mater.*, 2004, **14**, 38–44.
66 J. Mai, Y. Xiao, G. Zhou, J. Wang, J. Zhu, N. Zhao, X. Zhan and X. Lu, *Adv. Mater.*, 2018, **30**, 1802888.
67 Y. Xiao and X. Lu, *Mater. Today Nano*, 2019, **5**, 100030.
68 A. L. Patterson, *Phys. Rev.*, 1939, **56**, 978–982.

